

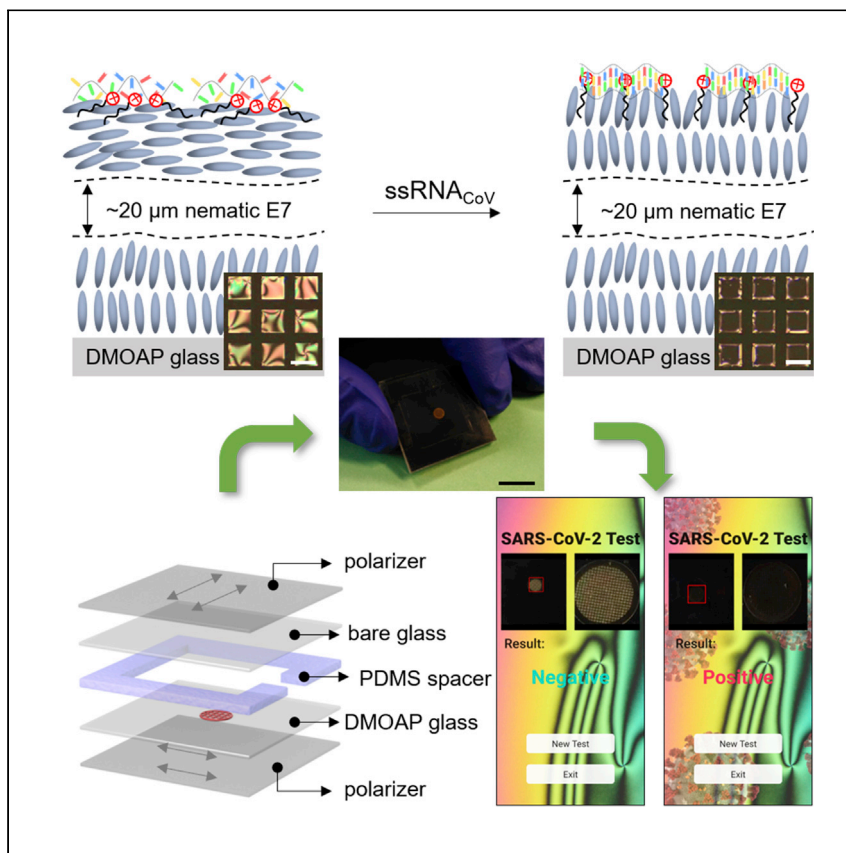


Since January 2020 Elsevier has created a COVID-19 resource centre with free information in English and Mandarin on the novel coronavirus COVID-19. The COVID-19 resource centre is hosted on Elsevier Connect, the company's public news and information website.

Elsevier hereby grants permission to make all its COVID-19-related research that is available on the COVID-19 resource centre - including this research content - immediately available in PubMed Central and other publicly funded repositories, such as the WHO COVID database with rights for unrestricted research re-use and analyses in any form or by any means with acknowledgement of the original source. These permissions are granted for free by Elsevier for as long as the COVID-19 resource centre remains active.

Article

Ultrasensitive and Selective Detection of SARS-CoV-2 Using Thermotropic Liquid Crystals and Image-Based Machine Learning



Xu et al. report that surfactant-laden liquid crystal (LC) films can detect ssRNA of SARS-CoV-2 with high selectivity and sensitivity. Combining polarized light microscopy work principle and machine learning technology, a LC-based diagnostic kit and a smartphone-based application (app) are developed to enable automatic detection of SARS-CoV-2 ssRNA.

Yang Xu, Adil M. Rather, Shuang Song, ..., Rongjun Qin, Xiaoping Bao, Xiaoguang Wang

qin.324@osu.edu (R.Q.)
bao61@purdue.edu (X.B.)
wang.12206@osu.edu (X.W.)

HIGHLIGHTS

Detection of ssRNA of SARS-CoV-2 using surfactant-laden liquid crystal (LC) films

Precise detection of nucleotide sequence with high selectivity and sensitivity

Develop LC-based diagnostic kit for naked-eye detection of SARS-CoV-2 ssRNA

Develop a smartphone application (app) to enable automatic detection of SARS-CoV-2 ssRNA



Article

Ultrasensitive and Selective Detection of SARS-CoV-2 Using Thermotropic Liquid Crystals and Image-Based Machine Learning

Yang Xu,^{1,7} Adil M. Rather,^{1,7} Shuang Song,^{2,7} Jen-Chun Fang,¹ Robert L. Dupont,¹ Ufuoma I. Kara,¹ Yun Chang,³ Joel A. Paulson,^{1,4} Rongjun Qin,^{2,5,6,*} Xiaoping Bao,^{3,*} and Xiaoguang Wang^{1,4,8,*}

SUMMARY

Rapid, robust virus-detection techniques with ultrahigh sensitivity and selectivity are required for the outbreak of the pandemic coronavirus disease 2019 (COVID-19) caused by the severe acute respiratory syndrome-coronavirus-2 (SARS-CoV-2). Here, we report that the femtomolar concentrations of single-stranded ribonucleic acid (ssRNA) of SARS-CoV-2 trigger ordering transitions in liquid crystal (LC) films decorated with cationic surfactant and complementary 15-mer single-stranded deoxyribonucleic acid (ssDNA) probe. More importantly, the sensitivity of the LC to the SARS ssRNA, with a 3-bp mismatch compared to the SARS-CoV-2 ssRNA, is measured to decrease by seven orders of magnitude, suggesting that the LC ordering transitions depend strongly on the targeted oligonucleotide sequence. Finally, we design a LC-based diagnostic kit and a smartphone-based application (app) to enable automatic detection of SARS-CoV-2 ssRNA, which could be used for reliable self-test of SARS-CoV-2 at home without the need for complex equipment or procedures.

INTRODUCTION

The outbreak of the coronavirus disease 2019 (COVID-19), caused by the novel severe acute respiratory syndrome-coronavirus-2 (SARS-CoV-2) virus, has spread rapidly and evolved into a global pandemic.^{1–3} SARS-CoV-2 has an incubation period of 2–7 days, during which infected individuals present no obvious symptoms,^{4,5} and the transmission of the SARS-CoV-2 virus has been shown to peak on or before symptom onset.^{6,7} To efficiently control such pre-symptomatic transmission, rapid, robust, and inexpensive tests should be performed on a large fraction of the population.^{3,8} Nucleic acid tests on the viral RNAs swabbed from a patient's throat or nasal passage, typically in the form of a reverse-transcription polymerase chain reaction (RT-PCR) test, are effective for the detection of the SARS-CoV-2 virus. This RT-PCR test is considered to be the “gold standard” for clinical diagnosis.^{8–10} A promising alternative approach to RT-PCR is the isothermal amplification method, which mainly contains two techniques: loop-mediated isothermal amplification (LAMP)¹¹ and recombinase polymerase amplification (RPA).¹² However, these methods require both long characterization time and specialized equipment.

Very recently, Cas12 and Cas13,¹³ gold nanoparticles,¹⁴ field-effect transistors (FETs),¹⁵ the plasmonic photothermal (PPT) effect,¹⁶ and column agglutination test (CAT) technologies¹⁷ have emerged as diagnostic tools for the detection of SARS-CoV-2. Although these diagnostic techniques are promising, each has its

¹William G. Lowrie Department of Chemical and Biomolecular Engineering, The Ohio State University, Columbus, OH 43210, USA

²Department of Civil, Environmental and Geodetic Engineering, The Ohio State University, Columbus, OH 43210, USA

³Davidson School of Chemical Engineering, Purdue University, West Lafayette, IN 47907, USA

⁴Sustainability Institute, The Ohio State University, Columbus, OH 43210, USA

⁵Department of Electrical and Computer Engineering, The Ohio State University, Columbus, OH 43210, USA

⁶Translational Data Analytics Institute, The Ohio State University, Columbus, OH 43210, USA

⁷These authors contributed equally

⁸Lead Contact

*Correspondence: qin.324@osu.edu (R.Q.), bao61@purdue.edu (X.B.), wang.12206@osu.edu (X.W.)

<https://doi.org/10.1016/j.xcrp.2020.100276>



own limitations. For example, the gold-nanoparticle-based technique is cost prohibitive for large-scale testing and requires improvements in its detection limit in order to reduce the required input amount of virus samples. Moreover, the FETs and PPT-effect-based diagnostic approaches require specialized analytical equipment for virus detection, and the CAT approach requires blood sample collection and centrifugation that depends on an established testing laboratory. Thus, the development of a low-cost, rapid, reliable, and simple diagnostic method for the self-detection of the SARS-CoV-2 virus remains elusive.

Thermotropic liquid crystals (LCs) exhibit unifying characteristics and behaviors that emerge from the long-range orientational order and mobility of their mesogenic constituents^{18,19} and have been broadly utilized in fast-switching electro-optical devices, such as liquid crystal displays (LCDs).²⁰ Over the past decade, a series of work has revealed the design of LC films and droplets that undergo orientational ordering transitions in response to a wide range of molecules adsorbed at an interface, including synthetic surfactants^{21–23} and polymers,^{24,25} phospholipids,^{26–29} peptides,³⁰ proteins,^{31–34} streptavidin,³⁵ bacterial toxins,³⁶ and deoxyribonucleic acid (DNA).^{37–41} For instance, single-stranded DNA (ssDNA) and double-stranded DNA (dsDNA) produce different orientations of LCs at cationic surfactant-laden aqueous-LC interfaces, which leads to a change in the effect on visible light caused by the optical birefringence of the LC film and thus enables the detection of DNA hybridization under polarized light microscopy.^{40,41} Despite the great potential of LC biosensor applications, their rational study and use in the detection of ribonucleic acid (RNA), which is the core genetic material of most pathogenic viruses, have not yet been explored.

In this study, we report the design of LC-based sensors for the reliable detection of SARS-CoV-2 RNA. Specifically, a partially self-assembled monolayer of cationic surfactants is formed at an aqueous-LC interface, followed by the adsorption of a 15-mer ssDNA probe with a complementary sequence to the SARS-CoV-2 virus at the cationic surfactant-laden aqueous-LC interface. We demonstrate that the ordering transition in the formed LC surface strongly depends on the targeted nucleotide sequence. The minimum concentration of SARS-CoV-2 RNA that can drive an ordering transition in the LC film is seven orders of magnitude lower than that of the base-pair-mismatched SARS RNA. Furthermore, we design and fabricate a LC-based SARS-CoV-2 RNA point-of-care detection kit, with an obtained response that is visible to the naked eye without any additional equipment, and a smartphone-based application (app) to enhance the overall accuracy of the test result readout and to avoid user error. Overall, these results unmask principles by which LCs and RNA can be coupled at cationic surfactant-decorated aqueous interfaces and hint at new routes by which the RNA of a pathogenic virus can be rapidly and easily sensed using LCs with both high sensitivity and selectivity.

RESULTS AND DISCUSSION

Preparation of the Cationic Surfactant-Decorated LC Films

The initial experiments reported below employed a cationic surfactant dodecyltrimethylammonium bromide (DTAB)-decorated interface on micrometer-thick films of nematic E7. The thermotropic LC E7 was chosen because of the relatively broad temperature range of its nematic mesophase (−62°C–58°C). In this phase, the rod-shaped E7 molecules have no positional order but self-align to possess a long-range orientational order. As described in the [Experimental Procedures](#) and in [Figure 1](#), films of nematic E7, with an approximately flat interface, were prepared by filling

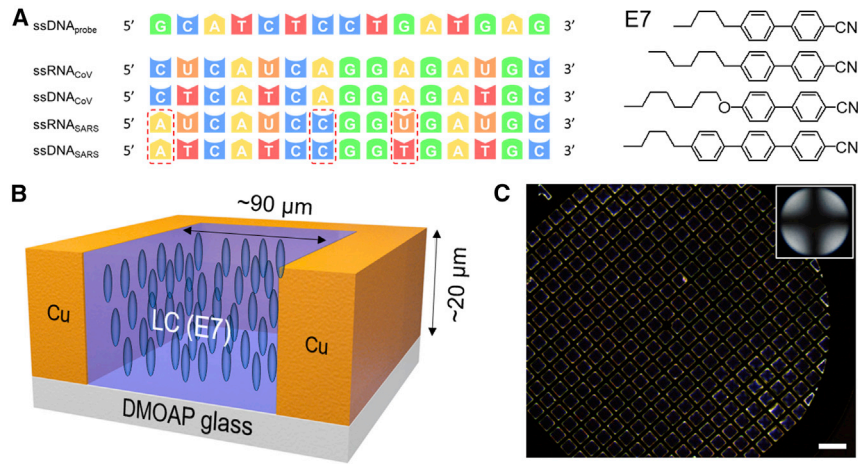


Figure 1. ssDNA/ssRNA Sequences and Grid-Infused LC Films

(A) Oligonucleotide sequence of ssDNA and ssRNA and the molecular structure of thermotropic LC E7.

(B) Schematic illustration of the E7-filled specimen grid on a DMOAP-functionalized glass slide.

(C) Representative optical micrograph (crossed polarizers) of the E7-filled specimen grid on a DMOAP-functionalized glass slide in air. Inset in (C) is a conoscopic image confirming homeotropic alignment of E7 in the film. Scale bar, 200 μm .

the pores of a 20- μm -thick copper specimen grid supported on a dimethyloctadecyl [3-(trimethoxysilyl) propyl]ammonium chloride (DMOAP)-functionalized glass slide, which induced a perpendicular ordering of the E7. Next, the E7 films were submerged into an aqueous solution of 5 mM sodium chloride (NaCl) (pH \sim 5.5–6.0), which was chosen to minimize the repulsive interaction of the base pairs of the ssDNA.⁴⁰

A monolayer of DTAB was subsequently deposited at the aqueous-E7 interface by adding an aqueous solution of DTAB to the aqueous phase above the E7 film. The DTAB was then allowed to adsorb onto the surface for 10 min. The optical images of DTAB-decorated E7 films were obtained by using an Olympus BX53 polarized light microscope equipped with crossed polarizers and set to the transmission mode. After adsorption of DTAB at the aqueous-E7 interface, we observed the optical appearance of the E7 films to be uniformly dark, which is consistent with the homeotropic anchoring of the nematic E7 at the DTAB-decorated aqueous interface of the E7 films (Figure 2A). Previous studies have established that steric interactions between the acyl tails of synthetic surfactants and mesogens cause LCs to adopt a homeotropic orientation.^{37,40} We comment here that, under the experimental condition of a 0.5 mM solution of DTAB, where the surface coverage of DTAB was near the minimum required for homeotropic orientation, we calculated only \sim 36% of the aqueous interface to be covered by DTAB (see Notes S1 and S2). These results suggest that a substantial open LC surface area exists at the interface and thus a LC re-orientation is allowed upon the adsorption of ssRNA and/or ssDNA at the interface. We also comment here that such low surface coverage of DTAB plays a critical role in the ultrasensitive detection of SARS-CoV-2, which will be discussed later.

Adsorption of the Probe ssDNA

Next, we deposited a 15-mer probe ssDNA (ssDNA_{probe}) (5'-GCATCTCTGATGAG-3'), which can hybridize with our target 15-mer SARS-CoV-2 ssRNA (ssRNA_{CoV}) (5'-CUCAUCAGGAGAUGC-3'), at the DTAB-decorated aqueous-E7 interface. The negatively charged ssDNA is attracted to the cationic DTAB at the aqueous-E7

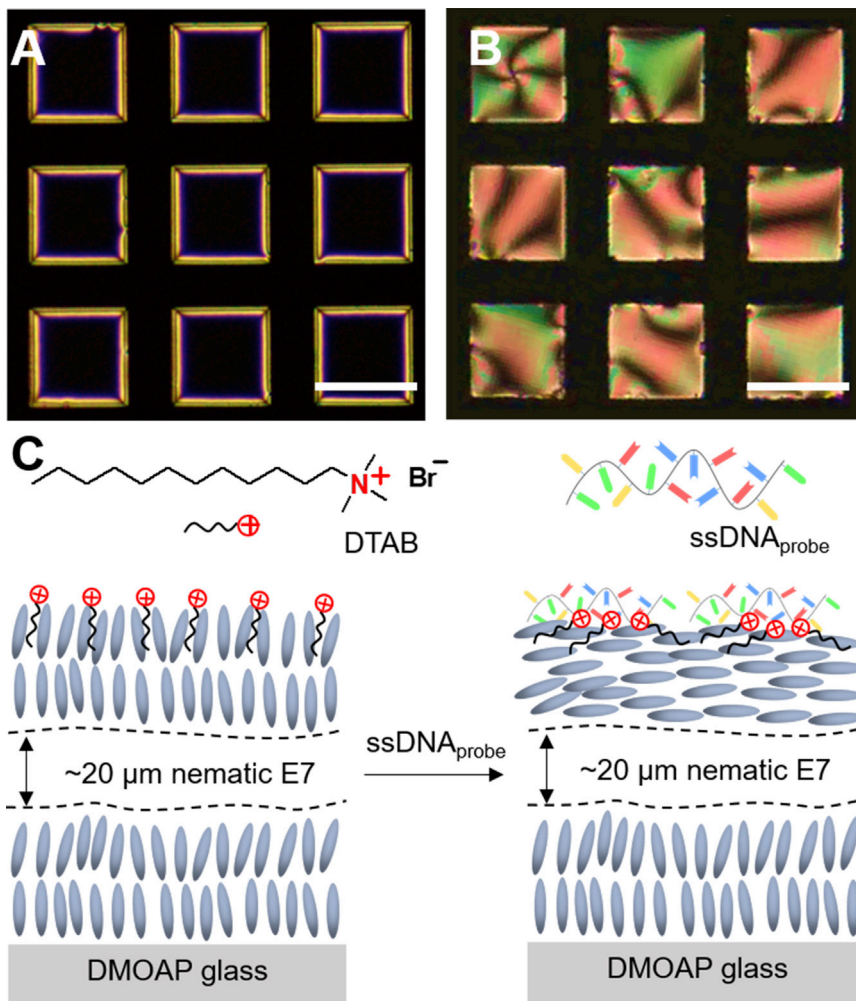


Figure 2. Adsorption of the Probe DNA at the Cationic Surfactant-Decorated Aqueous-LC Interface

(A and B) Optical micrographs (crossed polarizers) of the E7 film after the adsorption of (A) DTAB and the subsequent adsorption of (B) the ssDNA_{probe}. Scale bars, 100 μm.

(C) Schematic illustration of the optical response of the DTAB-decorated LC film to the adsorption of the ssDNA_{probe}.

interface via electrostatic interactions. The temperature of the system was kept at the melting temperature (T_m) of the ssDNA_{probe}, at which 50% of the nucleotide was annealed. Figure 2B shows the dynamic optical response of the DTAB-decorated nematic E7 film to the adsorption of ssDNA_{probe}. After addition of 100 nM ssDNA_{probe}, micrometer-sized domains with a bright optical appearance (corresponding to the regions of E7 with a tilted or planar alignment) nucleated at the interface. Subsequently, these domains grew over a period of 10 min, resulting in a bright optical appearance across the entire aqueous-E7 interface. These results indicate that, as the ssDNA_{probe} adsorbs to the interface, the flexible ssDNA_{probe} chains (with typical persistence length of ~ 6 Å)⁴² tend to spread at the surface and the hydrophobic bases of the ssDNA_{probe} interact with the DTAB to decrease the effective surface coverage of DTAB below what is required for a homeotropic orientation, resulting in a reorientation of the LC from homeotropic to either tilted or planar, as illustrated in Figure 2C. This phenomenon is consistent with previous

studies.^{37,41} The concentration of the ssDNA_{probe} was fixed at 100 nM for the rest of the experiments performed in this work. We emphasize here that the addition of 100 nM ssDNA_{probe} to E7 films incubated in a 6 mM DTAB solution (>90% of the aqueous-E7 interface is covered by DTAB; [Figure S1](#)) triggers no measurable change in the optical appearance of the E7 films, revealing that the surface coverage of DTAB plays a key role in driving the reorientation of the LC surface anchoring upon adsorption of the ssDNA_{probe}.

Detection of the SARS-CoV-2 ssRNA

In this set of experiments, we investigated the effect of the adsorption of ssRNA_{CoV} on the optical response of the ssDNA_{probe}/DTAB-decorated aqueous-E7 interfaces ([Video S1](#)). As shown in [Figure 3A](#), after addition of the ssRNA_{CoV} to the aqueous phase, black domains were observed to nucleate and grow on the E7 surface over a period of 20 min, resulting in a uniformly dark optical appearance that corresponds to the homeotropic anchoring of the nematic E7 across the entire aqueous-E7 interface. Furthermore, quantification of the optical appearance of the E7 films revealed a clear threshold concentration in a plot of normalized grayscale of E7 films versus ssRNA_{CoV} concentration ([Figures 3B and S2](#)). Inspection of [Figure 3D](#) shows that remarkably low concentrations of ssRNA_{CoV} (~30 fM of target ssRNA) are able to trigger the ordering transition of the E7 (see [Note S3](#) and [Figure S3](#)). In addition, the response time of the E7 film from a bright to dark optical appearance decreased with an increase in the concentration of ssRNA_{CoV}, as shown in [Figure 3E](#).

Our polarized light microscopy imaging revealed that the adsorption of ssRNA_{CoV} caused a LC reorientation from tilted/planar to homeotropic at the DTAB-decorated aqueous-E7 interface. We notice here that our results shown in [Figure 3C](#) are strikingly similar to past studies of the DNA hybridization at an aqueous-LC interface, where hybridization between a ssDNA_{probe} and a complementary targeted ssDNA caused a transition from a tilted/planar to a perpendicular orientation of the LCs at the cationic surfactant-decorated aqueous-LC interface.^{37,40,41} Building from the previous studies of the DNA hybridization at LC surfaces, we hypothesize that, upon adsorption of complementary ssRNA_{CoV} to the aqueous-E7 interface, the nucleobases of ssRNA_{CoV} will bind to its complementary base of the ssDNA_{probe} rather than remaining intercalated between the surfactant molecules due to the strong forces from hydrogen bonding and hydrophobic interactions involved in the process of hybridization. Once hybridized, the rigidity of the ssDNA-ssRNA complexes increase (e.g., the persistence length of the dsDNA increases by two orders of magnitude).^{42,43} Such an increase in the rigidity compacts the double strands of the ssRNA-ssDNA, and the hydrophobic bases are no longer exposed. Therefore, the rigid ssDNA-ssRNA complexes allow for a more efficient packing at the DTAB-decorated aqueous-E7 interface and thus reorganize the DTAB to the original surface coverage prior to the ssDNA_{probe} adsorption. This increase in effective surface coverage of DTAB gives rise to the transition from the planar/tilted orientation to the homeotropic orientation that is observed in our experiments.

Next, we performed two additional experiments to provide insight into the role of the target ssRNA on the ordering transition in LC films. First, we adsorbed pre-hybridized ssDNA_{probe}-ssRNA_{CoV} to the DTAB-decorated E7 films that were prepared as described earlier (see [Note S4](#)). At concentrations up to 100 nM, the presence of pre-hybridized ssDNA_{probe}-ssRNA_{CoV} had no measurable impact on the optical appearance of the E7 film ([Figure S4](#)). Second, we adsorbed complementary 15-mer SARS-CoV-2 ssDNA (ssDNA_{CoV}) (5'-CTCATCAGGAGATGC-3') to the ssDNA_{probe}/DTAB-decorated aqueous-E7 interface. Similar to the ssRNA_{CoV}, we

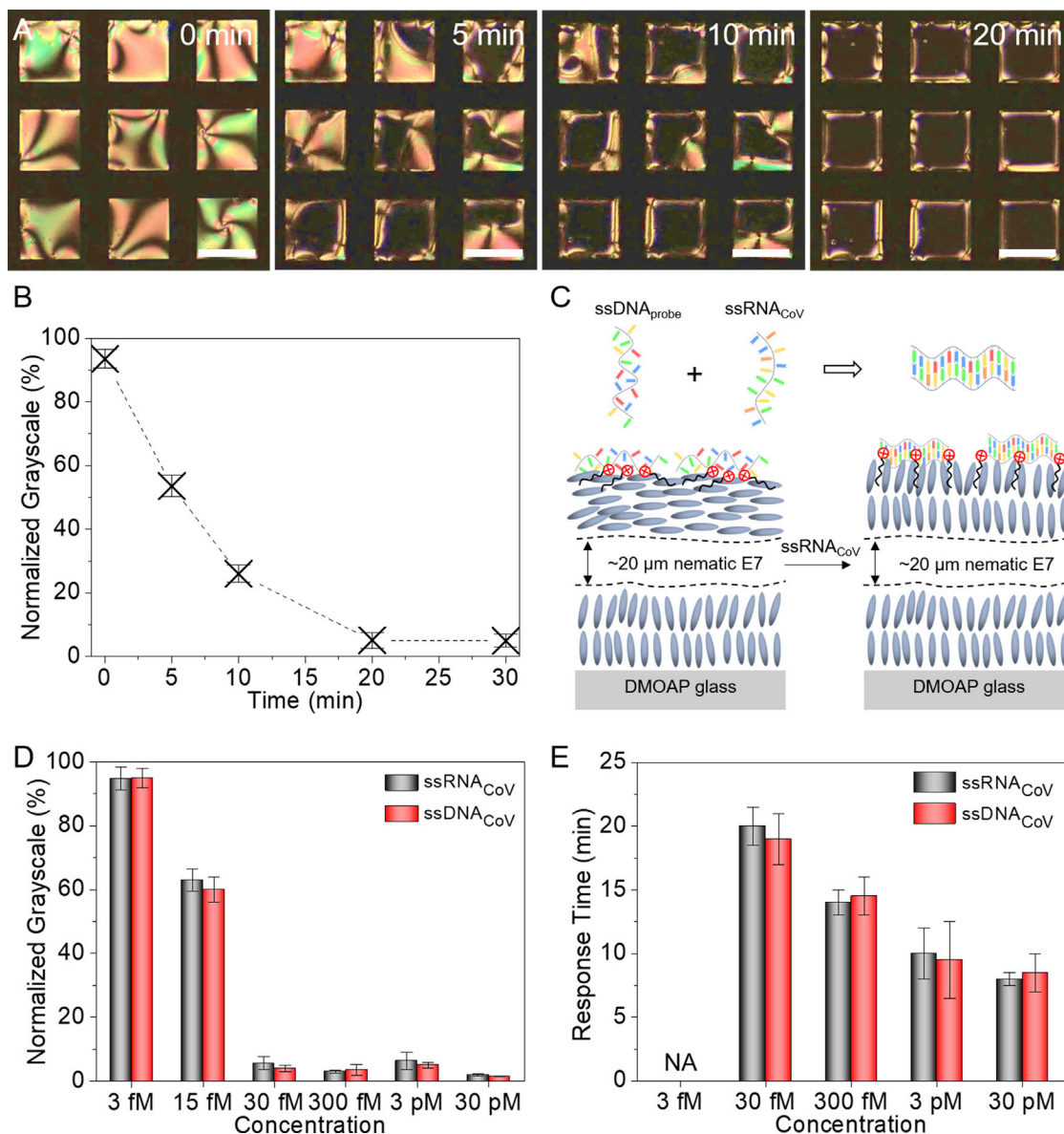


Figure 3. Adsorption of the SARS-CoV-2 RNA at the Aqueous-LC Interface

(A) Optical micrographs (crossed polarizers) of the dynamic response of the DTAB/ssDNA_{probe}-decorated E7 film to the adsorption of ssRNA_{CoV}. Scale bars, 100 μ m.

(B) Normalized grayscale of the E7 films upon adsorption of ssRNA_{CoV} as a function of time.

(C) Schematic illustration of the optical response of the DTAB/ssDNA_{probe}-decorated LC film to the adsorption of ssRNA_{CoV}.

(D and E) Normalized grayscale and response time of the DTAB/ssDNA_{probe}-decorated E7 films as a function of the concentration of ssRNA_{CoV} and ssDNA_{CoV}. The error bars are represented as mean of three separate measurements.

observed the ssDNA_{CoV} was able to trigger the ordering transition of the DTAB-decorated E7 film at remarkably low concentrations ($<10^2$ fM). We note here that the sensitivity of our DTAB-decorated E7 film (30 fM) is around three orders of magnitude higher than previous study on the detection of a ssDNA using a DTAB-decorated nematic LC film (50 pM).⁴¹ The ultrasensitivity of our LC films can be attributed to the minimum surface coverage of DTAB at the aqueous-E7 interface (0.5 mM) compared with the concentration of DTAB (several mM) in the previous study.⁴¹

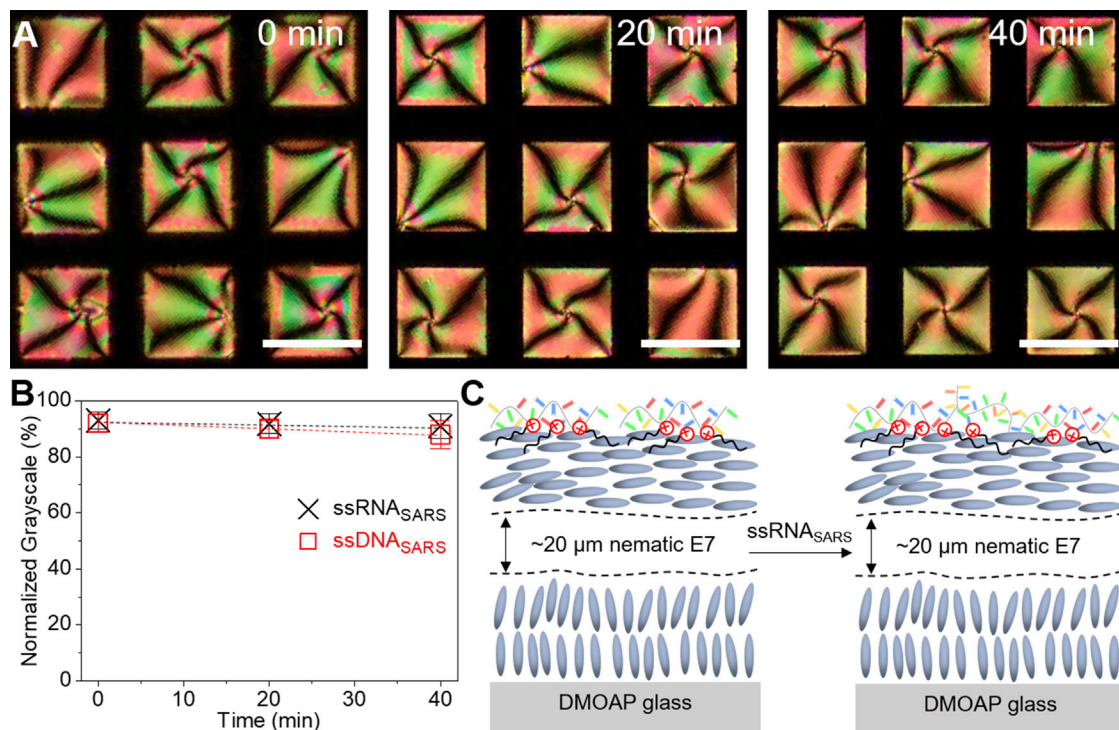


Figure 4. Adsorption of the SARS RNA at the Aqueous-LC Interface

(A) Optical micrographs (crossed polarizers) of the dynamic response of the DTAB/ssDNA_{probe}-decorated E7 film to the adsorption of ssRNA_{SARS}. Scale bars, 100 μ m.

(B) Normalized grayscale of the E7 films upon adsorption of ssRNA_{SARS} and ssDNA_{SARS} as a function of time.

(C) Schematic illustration of the optical response of the DTAB/ssDNA_{probe}-decorated LC film to the adsorption of ssRNA_{SARS}. The error bars are represented as mean of three separate measurements.

Selectivity of LC Films

To examine the selectivity of the obtained ssDNA_{probe}/DTAB-decorated E7 films, 15-mer ssRNAs or ssDNAs with different degrees of base pair mismatch were tested. The first oligonucleotide sequence tested was the SARS virus, a close member of the coronavirus family that emerged in 2003, with a nucleotide sequence 5'-AUC AUCGGUGAUGC-3' (ssRNA_{SARS}), which contains a 3-bp mismatch compared with the ssDNA_{probe}. As shown in Figure 4A, for concentrations up to 30 nM, we measured no change in the optical appearance of the ssDNA_{probe}/DTAB-decorated E7 films for 90 min upon adsorption of ssRNA_{SARS} (Video S2). When the concentration of ssRNA_{SARS} reached 100 nM, the E7 film underwent an optical change from bright to dark after 90 min, corresponding to an ordering transition of E7 from planar/tilted to perpendicular at the aqueous-E7 interface. Moreover, we observed similar results using ssDNA_{SARS} (Figure 4B). This pronounced difference in threshold concentration of ssRNA_{CoV} (30 fM) and ssRNA_{SARS} (100 nM) required to trigger ordering transitions within E7 films (seven orders of magnitude) leads us to hypothesis that lack of hybridization between the ssDNA_{probe} and ssRNA_{SARS}, due to the 3-bp mismatch, caused no increase in the effective surface coverage of DTAB to trigger the E7 ordering transition at the aqueous-E7 interface (Figure 4C). We notice here that 10 μ L of 30 fM ssRNA_{CoV} corresponds to $\sim 1.8 \times 10^5$ copies, which is comparable with the SARS-CoV-2 virus RNA copy number in real patient swab sample.⁶

To further test this hypothesis, we performed measurements with two additional 15-mer ssDNA sequences with different degrees of base pair mismatch: 7-bp mismatch

ssDNA (ssDNA_{7bpm}) (5'-AGCGTCCGGTGACGT-3') and 15-bp mismatch ssDNA (ssDNA_{15bpm}) (5'-AGACGACTTCTCGTA-3'). When the ssDNA concentration reached 100 nM, the ssDNA_{7bpm} triggered the optical change of the ssDNA_{probe}/DTAB-decorated E7 films after a period of 90 min, which is similar to the behavior of both ssDNA_{SARS} and ssRNA_{SARS}. Additionally, the ssDNA_{15bpm} failed to cause any measurable difference in the optical appearance of the E7 films over a wide concentration range (3 fM–100 nM) after 90 min. Overall, these results support our hypothesis that the response of the ssDNA_{probe}/DTAB-decorated LC film strongly depends on the targeted oligonucleotide sequence, which gives rise to an ultrahigh selectivity to complementary ssRNA_{CoV}.

Design of SARS-CoV-2 Detection Kit

In the final set of experiments for this study, we sought to design a point-of-care detection kit for SARS-CoV-2 that is visible to the human eye. We fabricated a 2.5 × 2.5 cm optical cell-based detection kit by pairing one bare glass slide and one DMOAP-functionalized glass slide each with a polarizer sheet. The two surfaces were then spaced apart with a 2-mm-thick poly(dimethylsiloxane) (PDMS) spacer, as shown in Figures 5A and 5B. An opening was conserved in the center and at one side of the PDMS spacer to allow for the analysis and the injection of the test samples, respectively. A copper specimen grid (transmission electron microscopy [TEM] grid) was placed on the surface of the DMOAP-functionalized glass slide and was subsequently filled with E7. The optical cell was then filled with a 5 mM NaCl aqueous solution containing the ssDNA_{probe} at a concentration of 100 nM. We notice here that TEM grid can stabilize LC film against dewetting by water, and our LC sensors exhibit good stability under water for at least 10 days. We also comment here that this LC detection kit is not reusable. The bright optical appearance was visible to the human eye. Subsequently, 2 μL of ssRNA_{CoV} or ssRNA_{SARS} was added to the detection kit. When viewed with natural (sunlight) or artificial (lamp) light, a significant decrease in the brightness of the specimen grid was observed upon the addition of a 30-fM ssRNA_{CoV} solution (Figure 5C) and no measurable difference in the optical appearance in the case of a 30-fM ssRNA_{SARS} aqueous solution (Figure 5D).

For most real-world applications, people may visualize the result of the detection kit either under different environmental illumination conditions or at different distances, resulting in uncertainty or even error in the test result readout. To address this limitation/challenge, we employed machine learning strategy to develop a smartphone app to provide a reliable readout of the test result of our LC-based SARS-CoV-2 detection kit. The objective of this app is to provide deterministic readings for non-expert users with no background knowledge in LC sensors by utilizing the capacity of machine learning models to encode the sophisticated and non-linear visual patterns for prediction. Specifically, we employed a support vector machine (SVM),⁴⁴ which is a supervised machine learning model that is often used for statistical classification wherein the goal is to identify to which category (in this case either “positive” or “negative”) a new observation belongs. Because observations are in the forms of images, a feature extraction method was designed to reduce the dimensionality of the input space. In particular, this method involves two main steps: (1) a template-matching algorithm⁴⁵ for locating the E7-infused grid and (2) the calculation of a reduced number of descriptions in terms of the standard deviation of the color value of each pixel (in Commission internationale de l'éclairage 1976 L*a*b* [CIELAB] color space) in a subdivided grid of the region of interest (see Note S5 and Figures S5–S10). The model was trained on a dataset of 88 images, with 29 positive examples and a variety of negative examples. The system is able to accurately

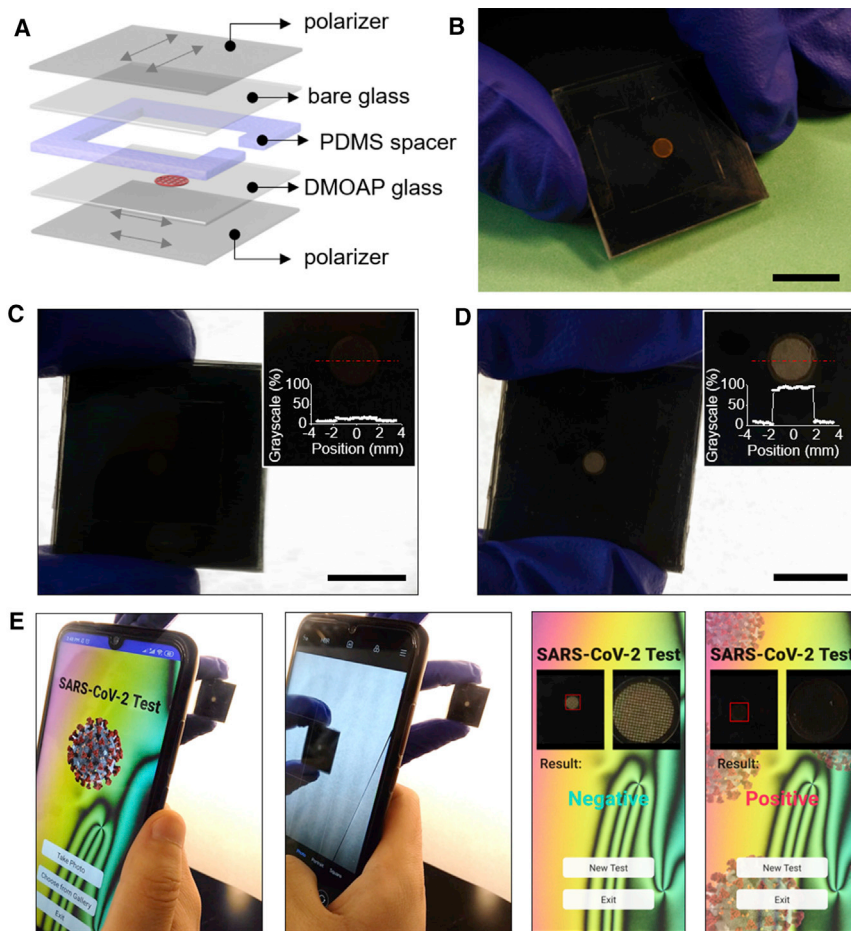


Figure 5. LC-Based Naked-Eye Home Detection Kit for SARS-CoV-2

(A and B) Design and photograph of a LC-based detection kit for ssRNA_{CoV}. (C and D) Optical appearance of the LC-based detection kit when viewed under a lamp upon addition of (C) 30 fM ssRNA_{CoV} and (D) 30 fM ssRNA_{SARS}. Scale bars, 1 cm. Insets show the normalized grayscale of the TEM grids upon the adsorption of ssRNA_{CoV}. (E) Test result readout by smartphone app for negative (upon adsorption of <100 nM ssRNA_{SARS}) and positive (upon adsorption of >30 fM ssRNA_{CoV}) test results.

distinguish between the positive and negative samples given an image of the E7-infused grid (Figure 5E; Video S3). Overall, these results unmask the ways by which the ssDNA_{probe} and complementary ssRNA_{CoV} can be coupled at a cationic surfactant-decorated aqueous-LC interface and hint at design principles by which the nucleotide sequence of pathogenic virus RNA can be rapidly and reliably sensed using LCs.

In conclusion, it was observed that the LC ordering transitions can be triggered by adsorbing ssRNA_{CoV} at a cationic surfactant/ssDNA_{probe} aqueous-LC interface in a manner that depends strongly on the targeted nucleotide sequence. Additionally, when the surface coverage of DTAB was near the minimum required for a homeotropic orientation of the LCs, the minimum concentration of ssRNA_{CoV} that can drive the ordering transitions in the E7 film are seven orders of magnitude lower than that of ssRNA_{SARS}. In comparison with conventional detection techniques, we find that ssRNA_{CoV}-driven ordering transitions in LC films exhibited ultrahigh sensitivity and selectivity. To the best of our knowledge, this is the first experimental evidence

that LC films can optically respond to adsorbed RNA on an interface. Our results suggest new principles for the naked-eye self-detection of viruses, including SARS-CoV-2, without requiring complex equipment or procedure.

In future work, we will investigate the selective LC detection on different SARS-CoV-2 genome sequences and similar control sequences with fewer base pair mismatches. Additionally, the massive detection of full-length SARS-CoV-2-RNA-containing patient samples will be performed in a biosafety level 3 (BSL-3) laboratory to validate its reliability. Moreover, the influence of the target ssRNA on the ordering transition of LC confined in droplets is being investigated. Future efforts will also seek to explore more sophisticated deep-learning methods for image analysis, such as convolutional neural networks (CNNs),⁴⁶ which have been successfully applied in LC chemical sensors,^{47,48} semiconductors,⁴⁹ and a variety of image-based medical diagnostic tests,⁵⁰ including X-rays, ultrasounds, and magnetic resonance imaging (MRI). The main advantage of CNNs is their inherent capability to learn more complex features directly from raw data—mitigating the need to use expert knowledge to define specific hand-crafted features as done as a proof of concept in this work.

EXPERIMENTAL PROCEDURES

Resource Availability

Lead Contact

Further information should be directed to and will be fulfilled by the lead contact, Xiaoguang Wang (email: wang.12206@osu.edu).

Materials Availability

This study did not generate new unique materials.

Data and Code Availability

Further requests for datasets and code should be directed to and will be fulfilled by the Lead Contact.

Materials

Thermotropic LC E7 was purchased from Jiangsu Hecheng Advanced Materials. DTAB, DMOAP (42 wt % in methanol), NaCl, and the 15-mer ssRNA sequences (SARS-CoV-2 RNA 5'-CUCAUCAGGAGAUGC-3'; 3-bp mismatch SARS RNA 5'-AUCAUCCGGUGAUGC-3') and 15-mer ssDNA sequences (probe DNA 5'-GCATC TCCTGATGAG-3', complementary SARS-CoV-2 DNA 5'-CTCATCAGGAGATGC-3', 3-bp mismatch SARS DNA 5'-ATCATCCGGTGATGC-3', 7-bp mismatch DNA 5'-AGCGTCCGGTGACGT-3', and 15-bp mismatch DNA 5'-AGACGACTTCTC GTA-3') were purchased from Sigma-Aldrich. Anhydrous ethanol was obtained from Decon Labs. Microscope slides (25 × 75 × 1 mm) were purchased from Fisher Scientific. Linear polarizer sheets were obtained from Thorlabs. Copper specimen grids (GG-200Cu; 3.05 mm in diameter and 20 μm thick) were purchased from Electron Microscopy Sciences. 8-chambered cover glass system was obtained from Cellvis. Sylgard 184 PDMS precursor and curing agent were purchased from Dow Corning. Water used in all experiments was purified using a Milli-Q water purification system (Simplicity C9210). Unless stated otherwise, purchased chemicals were used as received without further modification or purification.

Preparation of DMOAP-Functionalized Glass Substrates

Glass slides were washed with water and ethanol and then dried under stream of nitrogen gas. The DMOAP aqueous solution was prepared by dissolving 1.5 wt % of DMOAP in water. The washed glass slides were placed in the DMOAP aqueous

solution and were kept at 40°C for 30 min. Afterward, the slides were rinsed with water and ethanol three times. Finally, the DMOAP-functionalized glass slides were dried under a stream of nitrogen gas and stored in the dark for further use.

Preparation of LC-Infused Specimen Grids

A copper specimen grid was placed on the surface of a DMOAP-functionalized glass slide (7 × 7 mm). Next, 0.5 μL of E7 was placed on the specimen grid using a syringe with the excess E7 being removed with a capillary tube to obtain a uniform thin film. The obtained E7-infused specimen grid was observed under polarized light microscopy to confirm the homeotropic orientation of LC mesogens within the LC film. In this work, E7 was used due to its relatively high nematic-isotropic phase transition temperature.

Adsorption of DTAB at Aqueous-LC Interfaces

The E7-filled specimen grid on the DMOAP-functionalized glass slide was immersed into a 5 mM NaCl aqueous solution (pH ranged from 5.5 to 6.0) and was subsequently exposed to a 0.5 mM DTAB solution. The E7 mesogens adopted a perpendicular anchoring at the DTAB-laden aqueous-E7 interfaces.

Optical Microscopy Characterization of LC Interfaces

The optical appearance of the E7 film during adsorption of ssRNA/ssDNA at the aqueous-E7 interface was recorded using an Olympus BX53 polarized light microscope equipped with crossed polarizers. Images were captured using a charge-coupled device (CCD) camera.

Adsorption of Probe ssDNA

The probe ssDNA (ssDNA_{probe}) (15-mer-5'-GCATCTCCTGATGAG-3') was added to the DTAB-adsorbed E7 surface, and the optical response of the E7 surface was characterized with polarized light microscopy. The surface anchoring of E7 changed from homeotropic to planar/tilted within 5 min as the concentration of the ssDNA_{probe} reached 100 nM, resulting in a bright optical appearance.

Detection of the Target ssRNA/ssDNA

Here, we used SARS-CoV-2 ssRNA (ssRNA_{CoV}) (15-mer-5'-CUCAUCAGGAGAUGC-3') as an example. We added ssRNA_{CoV} to the DTAB-laden E7 surface with the adsorbed ssDNA_{probe}. The temperature of the system was increased to 48.7°C, which is the T_m of the ssRNA_{CoV}. A Linkam PE120 Peltier hot stage was used to control the temperature of the E7 surface during these measurements. We characterized the grayscale of the E7 film over a period of 40 min. To determine the detection limit of the E7 surface for the target ssRNA/ssDNA, we varied the concentration of the target ssRNA/ssDNA from nanomolar to femtomolar concentrations.

Characterization of the Surface Tension of DTAB-Adsorbed Aqueous-LC Interfaces

A KRÜSS DSA 100 goniometer was used to measure the surface tension of aqueous-E7 interfaces using a pendant drop method. During these measurements, E7 was pushed through a needle slowly, at 5 μL/min, to minimize the effect of the dynamic forces on the shape of the droplet. Images of the pendant E7 droplet near departure were captured and analyzed using a drop shape analyzer to estimate the surface tensions.

Quantification of the Optical Appearance of the LC Films

The optical appearance (i.e., brightness) of the RNA-adsorbed E7 films was quantified from images using ImageJ software. We set the grayscale of the E7 film upon adsorption of DTAB and the ssDNA_{probe} to be G_{DTAB} and G_{probe} , respectively. Upon addition of the target DNA/RNA, the grayscale of the E7 films, G , was measured and the rescaled grayscale value was calculated as

$$\text{Rescaled grayscale} = \frac{G - G_{DTAB}}{G_{probe} - G_{DTAB}} \quad (\text{Equation 1})$$

Fabrication of Detection Kit for SARS-CoV-2

A 2.5 × 2.5 cm optical cell-based detection kit was fabricated by combining one bare glass slide and one DMOAP-functionalized glass slide each with a polarizer sheet. These combined surfaces were then spaced apart using a 2-mm-thick PDMS spacer. An opening was conserved in the center and on one side of PDMS spacer to allow for the analysis and injection of test samples, respectively. A copper specimen grid was placed on the surface of the DMOAP-functionalized glass slide and was subsequently filled with E7.

Development of a Machine-Learning-Based, Smartphone-Based App for the Detection Kit

This app takes smartphone pictures of the LC-based detection kits and provides a test result about the SARS-CoV-2 virus. The algorithm first detects the LC-infused specimen grid location from the images using a multi-scale template-matching algorithm, which can be written as

$$\arg \min_{\Omega \in K, s} \int_{\Omega, s} |J(p) - \Psi(I(p))|^2 dp, \quad (\text{Equation 2})$$

where K is the full smartphone image space, I refers to a specific smartphone image, s refers to the scale of the template to accommodate smartphone images taken at different distance to the image, and Ω is a subset of the image space, which is parameterized by its location and shape. J is a template of the LC-infused specimen grid at a normalized size, and Ψ refers to a brightness invariant transformation to allow the LC-infused specimen grid location algorithm to operate on image under different lighting conditions. Here, we used the well-known Canny edge operator for Ψ .⁵¹

In a second step, we resized the detected LC film location Ω from the smartphone images to 128 × 128 pixels and subdivided them into 4 × 4 grids, with each grid having a size of 16 × 16 pixels (each pixel has three color channels). To allow robust feature extraction, we converted the red-green-blue (RGB) images to a more computationally friendly color space called CIELAB space,⁵² as it separates the illumination and chromatic components well. The variances of the pixel colors within each of the LC film were concatenated as a 48-dimensional feature vector (4 × 4 grids × 3 color channels), with each component normalized between 0 and 1. The support vector machine classifier⁴⁴ was trained on the 88 independent LC detection kit samples to classify the positive and negative samples based on the extracted variance vector.

SUPPLEMENTAL INFORMATION

Supplemental Information can be found online at <https://doi.org/10.1016/j.xcrp.2020.100276>.

ACKNOWLEDGMENTS

J.A.P. and X.W. thank the funding support from the startup funds of The Ohio State University (OSU), and X.W. thanks OSU Institute for Materials Research Kickstart Facility Grant. X.B. thanks the funding support from the startup funds of Davidson School of Chemical Engineering at Purdue University. S.S. and R.Q. thank the funding support from Office of Naval Research (ONR grant N00014-17-1-2928).

AUTHOR CONTRIBUTIONS

The experimental strategy was proposed initially by X.B. and X.W. and developed by all authors. Y.X., A.M.R., and J.-C.F. prepared the LC surface, performed material characterization, fabricated the LC detection kit, and collected the data. Y.X., A.M.R., J.-C.F., J.A.P., X.B., and X.W. co-analyzed the experimental data. S.S., J.A.P., and R.Q. discussed the machine learning ideas, and S.S. and R.Q. developed the smartphone app. All authors discussed the results and contributed to the final manuscript, and X.W. supervised the project.

DECLARATION OF INTERESTS

The Ohio State University has filed a patent application (application number 63066000) on the work described in this manuscript. The inventors listed on the patent application are X.W., X.B., R.Q., Y.X., and A.M.R. The authors declare no other competing interests.

Received: August 24, 2020

Revised: October 1, 2020

Accepted: November 6, 2020

Published: November 17, 2020

REFERENCES

- Chan, J.F.-W., Yuan, S., Kok, K.-H., To, K.K.-W., Chu, H., Yang, J., Xing, F., Liu, J., Yip, C.C.-Y., Poon, R.W.-S., et al. (2020). A familial cluster of pneumonia associated with the 2019 novel coronavirus indicating person-to-person transmission: a study of a family cluster. *Lancet* **395**, 514–523.
- Huang, C., Wang, Y., Li, X., Ren, L., Zhao, J., Hu, Y., Zhang, L., Fan, G., Xu, J., Gu, X., et al. (2020). Clinical features of patients infected with 2019 novel coronavirus in Wuhan, China. *Lancet* **395**, 497–506.
- Li, Q., Guan, X., Wu, P., Wang, X., Zhou, L., Tong, Y., Ren, R., Leung, K.S.M., Lau, E.H.Y., Wong, J.Y., et al. (2020). Early transmission dynamics in Wuhan, China, of novel coronavirus-infected pneumonia. *N. Engl. J. Med.* **382**, 1199–1207.
- Zhu, N., Zhang, D., Wang, W., Li, X., Yang, B., Song, J., Zhao, X., Huang, B., Shi, W., Lu, R., et al.; China Novel Coronavirus Investigating and Research Team (2020). A novel coronavirus from patients with pneumonia in China, 2019. *N. Engl. J. Med.* **382**, 727–733.
- Rothan, H.A., and Byrareddy, S.N. (2020). The epidemiology and pathogenesis of coronavirus disease (COVID-19) outbreak. *J. Autoimmun.* **109**, 102433.
- Wölfel, R., Corman, V.M., Guggemos, W., Seilmaier, M., Zange, S., Müller, M.A., Niemeyer, D., Jones, T.C., Vollmar, P., Rothe, C., et al. (2020). Virological assessment of hospitalized patients with COVID-2019. *Nature* **581**, 465–469.
- He, X., Lau, E.H.Y., Wu, P., Deng, X., Wang, J., Hao, X., Lau, Y.C., Wong, J.Y., Guan, Y., Tan, X., et al. (2020). Temporal dynamics in viral shedding and transmissibility of COVID-19. *Nat. Med.* **26**, 672–675.
- Wang, H., Li, X., Li, T., Zhang, S., Wang, L., Wu, X., and Liu, J. (2020). The genetic sequence, origin, and diagnosis of SARS-CoV-2. *Eur. J. Clin. Microbiol. Infect. Dis.* **39**, 1629–1635.
- Centers for Disease Control and Prevention (2020). Real-time RT-PCR panel for detection 2019-nCoV. <https://www.cdc.gov/coronavirus/2019-ncov/lab/rt-pcr-detection-instructions.html>.
- Yuan, X., Yang, C., He, Q., Chen, J., Yu, D., Li, J., Zhai, S., Qin, Z., Du, K., Chu, Z., and Qin, P. (2020). Current and perspective diagnostic techniques for COVID-19. *ACS Infect. Dis.* **6**, 1998–2016.
- Esbin, M.N., Whitney, O.N., Chong, S., Maurer, A., Darzacq, X., and Tjian, R. (2020). Overcoming the bottleneck to widespread testing: a rapid review of nucleic acid testing approaches for COVID-19 detection. *RNA* **26**, 771–783.
- Yan, C., Cui, J., Huang, L., Du, B., Chen, L., Xue, G., Li, S., Zhang, W., Zhao, L., Sun, Y., et al. (2020). Rapid and visual detection of 2019 novel coronavirus (SARS-CoV-2) by a reverse transcription loop-mediated isothermal amplification assay. *Clin. Microbiol. Infect.* **26**, 773–779.
- Broughton, J.P., Deng, X., Yu, G., Fasching, C.L., Servellita, V., Singh, J., Miao, X., Streithorst, J.A., Granados, A., Sotomayor-Gonzalez, A., et al. (2020). CRISPR-Cas12-based detection of SARS-CoV-2. *Nat. Biotechnol.* **38**, 870–874.
- Moitra, P., Alafeef, M., Dighe, K., Frieman, M.B., and Pan, D. (2020). Selective naked-eye detection of SARS-CoV-2 mediated by N gene targeted antisense oligonucleotide capped plasmonic nanoparticles. *ACS Nano* **14**, 7617–7627.
- Seo, G., Lee, G., Kim, M.J., Baek, S.H., Choi, M., Ku, K.B., Lee, C.S., Jun, S., Park, D., Kim, H.G., et al. (2020). Rapid detection of COVID-19 causative virus (SARS-CoV-2) in human nasopharyngeal swab specimens using field-effect transistor-based biosensor. *ACS Nano* **14**, 5135–5142.
- Qiu, G., Gai, Z., Tao, Y., Schmitt, J., Kullak-Ublick, G.A., and Wang, J. (2020). Dual-functional plasmonic photothermal biosensors for highly accurate severe acute respiratory syndrome coronavirus 2 detection. *ACS Nano* **14**, 5268–5277.

17. Alves, D., Curvello, R., Henderson, E., Kesarwani, V., Walker, J.A., Leguizamon, S.C., McLiesh, H., Raghuvanshi, V.S., Samadian, H., Wood, E.M., et al. (2020). Rapid gel card agglutination assays for serological analysis following SARS-CoV-2 infection in humans. *ACS Sens.* *5*, 2596–2603.
18. Kléman, M., and Lavrentovich, O.D. (2003). *Soft Matter Physics: An Introduction* (Springer).
19. Schenning, A., Crawford, G.P., and Broer, D.J. (2018). *Liquid Crystal Sensors* (CRC).
20. Rasing, T.h., and Musevic, I. (2004). *Surfaces and Interfaces Liquid Crystals* (Springer).
21. Concellón, A., Zentner, C.A., and Swager, T.M. (2019). Dynamic complex liquid crystal emulsions. *J. Am. Chem. Soc.* *141*, 18246–18255.
22. Miller, D.S., Wang, X., Buchen, J., Lavrentovich, O.D., and Abbott, N.L. (2013). Analysis of the internal configurations of droplets of liquid crystal using flow cytometry. *Anal. Chem.* *85*, 10296–10303.
23. Moreno-Razo, J.A., Sambriski, E.J., Abbott, N.L., Hernández-Ortiz, J.P., and de Pablo, J.J. (2012). Liquid-crystal-mediated self-assembly at nanodroplet interfaces. *Nature* *485*, 86–89.
24. Zou, J., and Fang, J. (2011). Adhesive polymer-dispersed liquid crystal films. *J. Mater. Chem.* *21*, 9149–9153.
25. Kinsinger, M.I., Buck, M.E., Abbott, N.L., and Lynn, D.M. (2010). Immobilization of polymer-decorated liquid crystal droplets on chemically tailored surfaces. *Langmuir* *26*, 10234–10242.
26. Brake, J.M., Daschner, M.K., Luk, Y.Y., and Abbott, N.L. (2003). Biomolecular interactions at phospholipid-decorated surfaces of liquid crystals. *Science* *302*, 2094–2097.
27. Zhao, Y., Mahajan, N., Lu, R., and Fang, J. (2005). Liquid-crystal imaging of molecular-tilt ordering in self-assembled lipid tubules. *Proc. Natl. Acad. Sci. USA* *102*, 7438–7442.
28. Cumberland, J., Lopatkina, T., Murachver, M., Popov, P., Kenderesi, V., Buka, A., Mann, E.K., and Jáklí, A. (2018). Bending nematic liquid crystal membranes with phospholipids. *Soft Matter* *14*, 7003–7008.
29. Manna, U., Zayas-Gonzalez, Y.M., Carlton, R.J., Caruso, F., Abbott, N.L., and Lynn, D.M. (2013). Liquid crystal chemical sensors that cells can wear. *Angew. Chem. Int. Ed. Engl.* *52*, 14011–14015.
30. Wang, X., Yang, P., Mondiot, F., Li, Y., Miller, D.S., Chen, Z., and Abbott, N.L. (2015). Interfacial ordering of thermotropic liquid crystals triggered by the secondary structures of oligopeptides. *Chem. Commun. (Camb.)* *51*, 16844–16847.
31. Hartono, D., Xue, C.-Y., Yang, K.-L., and Yung, L.-Y.L. (2009). Decorating liquid crystal surfaces with proteins for real-time detection of specific protein-protein binding. *Adv. Funct. Mater.* *19*, 3574–3579.
32. Zhu, Q., and Yang, K.-L. (2013). Amplification of interference color by using liquid crystal for protein detection. *Appl. Phys. Lett.* *103*, 243701.
33. Zhang, W., Ang, W.T., Xue, C.Y., and Yang, K.L. (2011). Minimizing nonspecific protein adsorption in liquid crystal immunoassays by using surfactants. *ACS Appl. Mater. Interfaces* *3*, 3496–3500.
34. Daschner De Tercero, M., and Abbott, N.L. (2008). Ordering transitions in liquid crystals permit imaging of spatial and temporal patterns formed by proteins penetrating into lipid-laden interfaces. *Chem. Eng. Commun.* *196*, 234–251.
35. Eimura, H., Miller, D.S., Wang, X., Abbott, N.L., and Kato, T. (2016). Self-assembly of bioconjugated amphiphilic mesogens having specific binding moieties at aqueous-liquid crystal interfaces. *Chem. Mater.* *28*, 1170–1178.
36. Lin, I.H., Miller, D.S., Bertics, P.J., Murphy, C.J., de Pablo, J.J., and Abbott, N.L. (2011). Endotoxin-induced structural transformations in liquid crystalline droplets. *Science* *332*, 1297–1300.
37. McUmber, A.C., Noonan, P.S., and Schwartz, D.K. (2012). Surfactant–DNA interactions at the liquid crystal–aqueous interface. *Soft Matter* *8*, 4335–4342.
38. Lai, S.L., Hartono, D., and Yang, K.-L. (2009). Self-assembly of cholesterol DNA at liquid crystal/aqueous interface and its application for DNA detection. *Appl. Phys. Lett.* *95*, 153702.
39. Zhou, J., Dong, Y., Zhang, Y., Liu, D., and Yang, Z. (2016). The assembly of DNA amphiphiles at liquid crystal–aqueous interface. *Nanomaterials (Basel)* *6*, 229–238.
40. Price, A.D., and Schwartz, D.K. (2008). DNA hybridization-induced reorientation of liquid crystal anchoring at the nematic liquid crystal/aqueous interface. *J. Am. Chem. Soc.* *130*, 8188–8194.
41. Khan, M., Khan, A.R., Shin, J.H., and Park, S.Y. (2016). A liquid-crystal-based DNA biosensor for pathogen detection. *Sci. Rep.* *6*, 22676.
42. Cui, S., Yu, Y., and Lin, Z. (2009). Modeling single chain elasticity of single-stranded DNA: A comparison of three models. *Polymer* *50*, 930–935.
43. Mandelkern, M., Elias, J.G., Eden, D., and Crothers, D.M. (1981). The dimensions of DNA in solution. *J. Mol. Biol.* *152*, 153–161.
44. Wang, L. (2005). *Support Vector Machines: Theory and Applications* (Springer).
45. Atallah, M.J. (2001). Faster image template matching in the sum of the absolute value of differences measure. *IEEE Trans. Image Process.* *10*, 659–663.
46. Lo, S.-C.B., Chan, H.-P., Lin, J.-S., Li, H., Freedman, M.T., and Mun, S.K. (1995). Artificial convolution neural network for medical image pattern recognition. *Neural Netw.* *8*, 1201–1214.
47. Cao, Y., Yu, H., Abbott, N.L., and Zavala, V.M. (2018). Machine learning algorithms for liquid crystal-based sensors. *ACS Sens.* *3*, 2237–2245.
48. Smith, A.D., Abbott, N., and Zavala, V.M. (2020). Convolutional network analysis of optical micrographs for liquid crystal sensors. *J. Phys. Chem. C* *124*, 15152–15161.
49. O’Leary, J., Sawlani, K., and Mesbah, A. (2020). Deep learning for classification of the chemical composition of particle defects on semiconductor wafers. *IEEE Trans. Semicond. Manuf.* *33*, 72–85.
50. Anwar, S.M., Majid, M., Qayyum, A., Awais, M., Alnowami, M., and Khan, M.K. (2018). Medical image analysis using convolutional neural networks: a review. *J. Med. Syst.* *42*, 226.
51. Canny, J. (1986). A computational approach to edge detection. *IEEE Trans. Pattern Anal. Mach. Intell.* *8*, 679–698.
52. Joblove, G.H., and Greenberg, D. (1978). Color spaces for computer graphics. *Comput. Graph.* *12*, 20–25.